

Wall-modeled large-eddy simulation of non-equilibrium turbulent boundary layers

By M. Cho, G. I. Park[†], A. Lozano-Durán AND P. Moin

1. Introduction

Large-eddy simulation (LES) has become an essential tool for both fundamental studies and real-world engineering applications. However, industrial use of LES has been hampered by its prohibitive grid-point requirements near the wall. This limitation motivates the need for wall models to perform LES at a reduced cost by modeling small-scale near-wall eddies, while resolving large-scale eddies in the outer region (Bose & Park 2018; Chapman 1979; Choi & Moin 2012). Although wall-modeled LES (WMLES) has emerged as a viable alternative to the computationally more expensive wall-resolved LES (Slotnick *et al.* 2014), the performance of wall models in non-equilibrium three-dimensional flows has not yet been carefully assessed. This assessment is particularly important as the most widely used wall models to date are built on equilibrium assumptions.

An example in which non-equilibrium effects emerge are three-dimensional turbulent boundary layers (3DTBLs). 3DTBLs have skewed mean velocity profiles, which can be caused by the lateral motion of the walls or the spanwise pressure gradient imposed by the bounding geometry. These 3DTBLs exist in a variety of practical problems, such as the bow and stern regions of a ship, curved ducts, and turbomachinery, among others. From the point of view of WMLES, 3DTBLs have peculiar features that are challenging to model, such as the misalignment of the Reynolds shear stress and the mean shear stress (Cho *et al.* 2018).

Recently, WMLES of a temporally-developing 3DTBL in a channel flow with a sudden imposition of spanwise pressure gradient was conducted by Giometto *et al.* (2017) and Lozano-Durán *et al.* (2020). The authors considered three wall models approaches: an ordinary-differential-equation (ODE)-based equilibrium wall model (Kawai & Larsson 2012), an integral non-equilibrium wall model (Yang *et al.* 2015), and a partial-differential-equation-based non-equilibrium wall model (Park & Moin 2014). The performance of the wall models was assessed in the transient channel flow at $Re_\tau = u_\tau h / \nu \approx 1000$, where u_τ is the wall-shear velocity, h is the channel half-height, and ν is the kinematic viscosity. Lozano-Durán *et al.* (2020) quantified the accuracy in predicting the magnitude and direction of the wall stress as the complexity of the wall model increases, and concluded that equilibrium models provide the best trade-off between accuracy and cost. A slip-velocity model (Bae *et al.* 2018) showed similar performance to the ODE based equilibrium wall model. In addition to this flow configuration, Cho *et al.* (2018) examined the performance of the ODE based equilibrium wall model for a spatially-developing 3DTBL inside a bent square duct at $Re_\tau = 1200 - 2400$, following the experiment of Schwarz & Bradshaw (1994). The authors reported a fairly good prediction of velocity and pressure distributions, with a measurable discrepancy of the crossflow

[†] University of Pennsylvania, Philadelphia PA

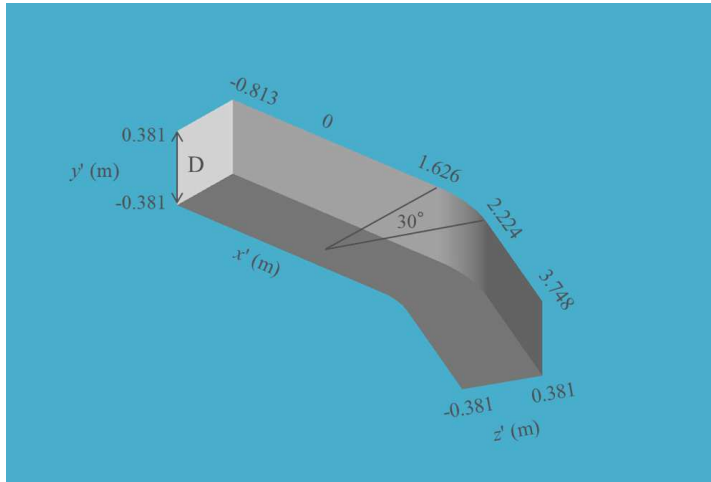


FIGURE 1. Flow configuration of the bent square duct. Here, the coordinate system (x', y', z') is aligned with the local duct centerline.

angles in the bend region. However, only one WMLES mesh was considered without a grid convergence study.

Another important example of non-equilibrium flows can be found in separated turbulent boundary layers. These 3D separated flows are common in engineering applications, and their accurate prediction is critical during the designing process. Nonetheless, it is unclear if separated regions should be tackled with WMLES, and the question of whether a wall model is needed in the separated region remains unknown. The recent review by Bose & Park (2018) has also pointed out that the use of the no-slip boundary condition might be justified in the separated region since there the flow is governed by slow and large-scale eddies. In that case, it remains to establish how to switch between the no-slip and wall model boundary conditions.

In this brief, we first report the performance of the ODE-based equilibrium wall model in a spatially-developing 3DTBL inside a bent square duct, which is complemented with a mesh convergence study in Section 2. In Section 3, we assess the ODE-based equilibrium wall model for LES predictions of 3D separated flows. Recent experimental studies by Ching *et al.* (2018a) on flows over a wall-mounted skewed bump with 3D flow separations are chosen for comparison purposes. Concluding remarks are offered in Section 4.

2. WMLES of a spatially-developing 3DTBL in a bent square duct

2.1. Computational details

Figure 1 shows the flow configuration of the bent square duct. The square duct has a $0.762\text{m} \times 0.762\text{m}$ cross-section and a streamwise length of 4.561 m. A spatially-developing 3DTBL is generated by a 30° bend that imposes a cross-stream pressure gradient. The surface streamlines are deflected by up to 22° relative to the centerline velocity vector. Then, the developed 3DTBL gradually recovers to a two-dimensional flow downstream of the bend. Following the experiment by Schwarz & Bradshaw (1994), two coordinate systems are defined in the present study (see Figure 1). The coordinate system (x, y, z) is aligned with the upstream section of the bend, where x , y , and z denote the streamwise, wall-normal, and spanwise directions, respectively. The other coordinate system (x', y', z')

TABLE 1. Case setup for the bent square duct

Case	Δs (m)	N_{CV}	N_δ	$N_{\delta,\text{bend}}$
D1	0.0025–0.01	30,400,000	8–11	9
D2	0.0025–0.01	38,000,000	8–15	13–15
D3	0.00125–0.01	76,400,000	8–24	24

is aligned with the local duct centerline. (U, V, W) are the corresponding mean velocity components for both coordinate systems.

WMLES is conducted using the code CharLES with Voronoi mesh generator (Brès *et al.* 2018). CharLES solves the compressible LES equations with constant-coefficient Vreman model as the SGS model. The unstructured Voronoi mesh generator, based on a hexagonal close packed (HCP) point-seeding method, can automatically build high-quality meshes for arbitrarily complex geometries with minimal user input. First, a surface geometry of the square duct is needed to describe the computational domain, as shown in Figure 1. Second, the user specifies the coarsest grid resolution of the uniformly seeded HCP points, Δs_{max} . For the present WMLES, Δs_{max} is set to 0.01 m and three different mesh refinements are considered, as shown in Table 1. For case D1, the meshes are refined in the near-wall region so that the number of grid cells across the local boundary layer thickness (N_δ) ranges from 8 to 11 along the streamwise direction. The minimum cell size in the wall units is $\Delta s_{\text{min}}^+ = \Delta s_{\text{min}} u_\tau / \nu = 140$, and 30.4 million control volumes are used in total. Case D2 has additional grid refinement, such that the number of control volumes across the boundary layer thickness within the bend section ($N_{\delta,\text{bend}}$) increases from 9 (case D1) to 13 to 15 (case D2) using 38 million control volumes. In the finest grid resolution (case D3), Δs_{min} is further reduced to 0.00125 m, resulting in $N_{\delta,\text{bend}} = 24$ using 76.4 million control volumes.

The wall-shear stress from the ODE-based equilibrium wall model (Kawai & Larsson 2012) is imposed as the boundary condition at the bottom, top, and side walls. The walls are assumed to be isothermal. At the matching location of the equilibrium wall model, temporally-filtered LES data are provided to the wall model as suggested by Yang *et al.* (2017). The characteristic-based non-reflective outflow boundary condition is imposed at the outflow plane (Poinsot & Lele 1992). For the inflow boundary condition, a synthetic turbulence boundary condition is imposed to provide a realistic turbulent inflow condition that matches the experiment in the upstream section of the bend (see Figure 2). The Reynolds number based on the duct side length ($D = 0.762$ m) and the inlet freestream velocity (26.5 m/s) is 1,400,000. The Reynolds number based on the local momentum thickness and the freestream velocity ranges from 4,000 to 9,000 ($Re_\tau = 1, 200 - 2, 400$).

2.2. Results and discussion

Figure 2 shows the profile of the mean velocity magnitude ($Q = \sqrt{U^2 + W^2}$) normalized with the freestream value (Q_∞) as a function of the wall-normal distance at various streamwise locations. The velocity profiles from three grids (i.e., cases D1, D2, and D3) are almost on top of each other at each streamwise location, which indicates that the WMLES solution has reached grid convergence. For comparison, the results of the no-slip

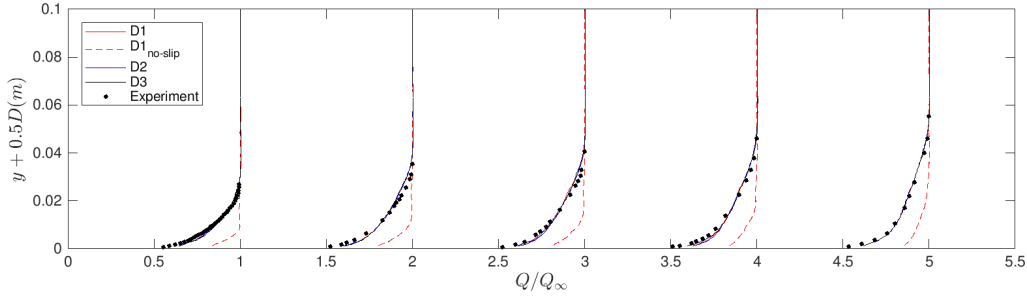


FIGURE 2. Mean velocity profiles at $x' = 0.978$ m (upstream section of the bend), $x' = 1.775$ m and 2.075 m (inside the bend), and $x' = 2.415$ m and 2.948 m (downstream section of the bend). Here, the profiles at $x' = 1.775$, 2.075 , 2.415 , and 2.948 m are shifted by 1, 2, 3, and 4 on the horizontal axis, respectively. Lines, present WMLES (cases D1, D2, D3); circles, experiment (Schwarz & Bradshaw 1994); dashed lines, no-slip LES on the case D1 mesh (without wall model).

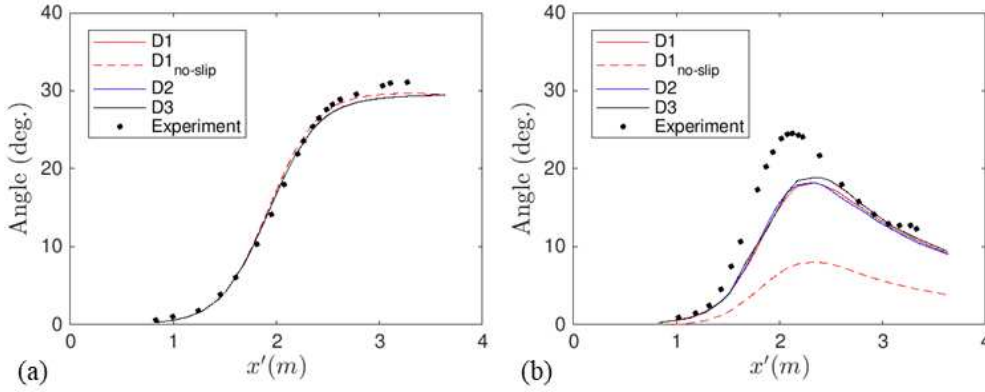


FIGURE 3. Crossflow turning angles: (a) freestream turning angle (γ_∞) distribution along the streamwise direction (x'); (b) surface crossflow angle relative to freestream ($\gamma_s - \gamma_\infty$) along the streamwise direction (x'). Lines, present WMLES (cases D1, D2, D3); circles, experiment (Schwarz & Bradshaw 1994); dashed lines, no-slip LES on the case D1 mesh (without wall model).

LES (without wall model) using the same coarse mesh for case D1 are also included in the figure.

In the upstream section of the bend at $x' = 0.978$ m, the WMLES solution reproduces the upstream condition of the reference experiment. The mean velocity magnitude profiles inside the bend (at $x' = 1.775$ m and 2.075 m) and downstream section (at $x' = 2.415$ m and 2.948 m) are also predicted with reasonable accuracy. On the other hand, the discrepancy between the experimental data and the result from no-slip LES is remarkable, indicating the importance of deploying the wall model at the present grid resolutions.

Crossflow turning angles are defined as $\gamma = \tan^{-1} W/U$, where W and U are spanwise and streamwise mean velocity components with respect to the upstream coordinate (x, y, z) . Their variations along the axial and wall-normal directions are represented in Figures 3 and 4, respectively. Here, γ_∞ is γ at the freestream, while γ_s is that at the surface. γ_∞ turns from 0° before the bend to 30° after the bend in accordance with

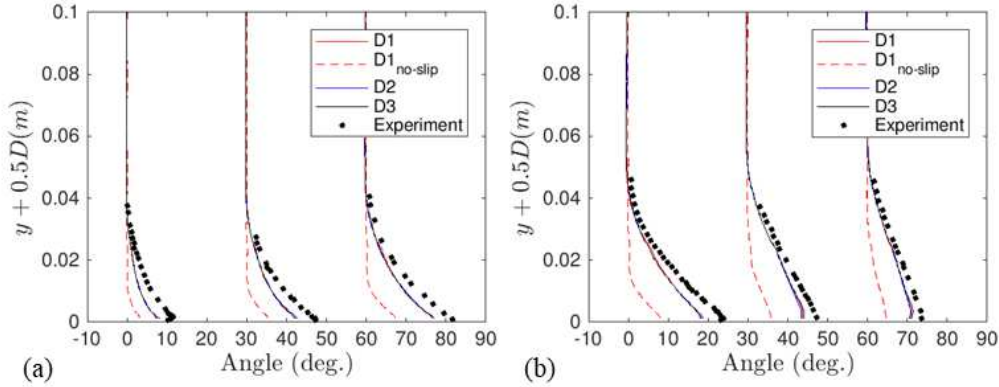


FIGURE 4. Crossflow angle relative to freestream: (a) crossflow inside the bend at $x'(m) = 1.676, 1.875,$ and 2.075 ; (b) crossflow in the downstream section of the bend at $x'(m) = 2.338, 2.948,$ and 3.329 . Here, the profiles at $x' = 1.875$ and 2.948 m are shifted by 30° and the profiles at $x' = 2.075$ and 3.329 m are shifted by 60° on the horizontal axis, respectively. Lines, present WMLES (cases D1, D2, D3); circles, experiment (Schwarz & Bradshaw 1994); dashed lines, no-slip LES on the case D1 mesh (without wall model).

the specified geometry, and the results from both WMLES (cases D1, D2, and D3) and no-slip LES on the case D1 mesh are almost on top of each other at this freestream wall-normal location. This is owing to the fact that the inviscid mechanisms dominate in the core region of the square duct. Also, the flow turning angles at the freestream wall-normal location (γ_∞) from both the WMLES and no-slip LES calculations show excellent agreement with the experiment.

The increase of the surface crossflow in the upstream and bend sections and its gradual decrease are captured from the current WMLES for all the cases D1, D2, and D3, but the magnitude of $\gamma_s - \gamma_\infty$ is underpredicted near the bend region. The result from case D3 is slightly better than for cases D1 and D2, but the difference is marginal. Here, the maximum value of γ_s is larger than the 30° bend angle, and this shows the effect of the cross-stream pressure gradient generated by the bend on the surface streamline direction. Also, the differences between the current WMLES and experiment are observed within the bend, but these differences decrease as the 3DTBL inside the bend gradually recovers to the two-dimensional turbulent boundary layer in the downstream section.

Figure 4 shows the crossflow angle relative to the freestream flow with respect to the wall-normal direction. The crossflow angle increases until the end of the bend section (Figure 4(a)) and decays in the downstream section (Figure 4(b)). Figure 4 also shows that the current WMLES can predict the crossflow development and decay, although the predicted angles are smaller than those in the experiment. Consistent with Figure 3, the discrepancy between the current WMLES and the experiment in $\gamma - \gamma_\infty$ increases with the crossflow development and then decreases with its decay. Also, in Figures 3 and 4, it is shown that no-slip LES significantly underperforms WMLES.

3. WMLES of a 3D flow separation behind a skewed bump

3.1. Computational details

Figure 5 illustrates the present three-dimensional skewed bump. The bump is mounted on the bottom wall of the square duct and its surface is defined by (Ching *et al.* 2018a,b;

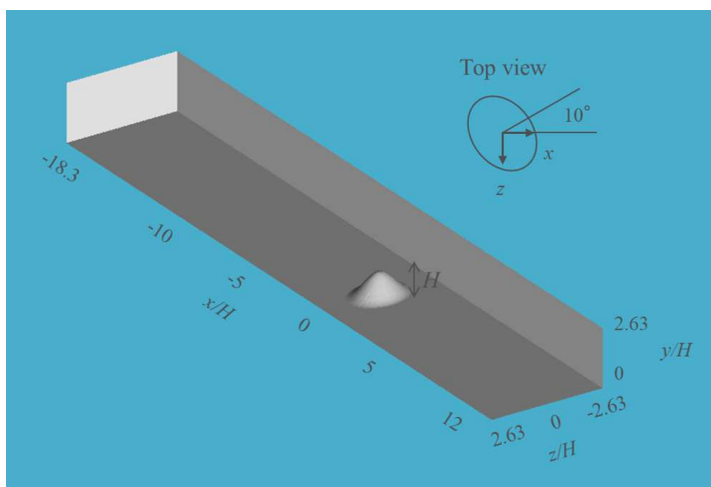


FIGURE 5. Flow configuration of the skewed bump. The coordinate origin is located on the bottom wall under the center of the bump.

TABLE 2. Case setup for the skewed bump

Case	$\Delta s/H$	N_{CV}	$N_{\delta, x/H=-4}$
B1	0.025–0.1	6,700,000	20
B2	0.012–0.1	19,000,000	20
B3	0.006–0.1	10,800,000	20
B4	0.006–0.1	22,300,000	20

Ching & Eaton 2019)

$$y_s = H \left[0.5 + 0.5 \cos \left(2\pi \sqrt{\frac{x_s^2}{b^2} + \frac{z_s^2}{a^2}} \right) \right], \quad (3.1)$$

for $\frac{x_s^2}{b^2} + \frac{z_s^2}{a^2} < \frac{1}{4}$, where x_s, y_s and z_s denote the surface of the bump in the streamwise, wall-normal, and spanwise directions, respectively; $H (= 19\text{mm})$ indicates the bump height, $a = 57\text{ mm}$, and $b = 42.75\text{ mm}$. Here, x_s and z_s are defined with respect to the bump rotation angle θ as

$$x_s = x \cos(\theta) + z \sin(\theta) \quad (3.2)$$

$$z_s = x \sin(\theta) - z \cos(\theta). \quad (3.3)$$

The bump angle in the present study is at $\theta = 10^\circ$ and the simulation results are compared with those of previous experimental and LES studies (Ching *et al.* 2018a; Ching & Eaton 2019). The coordinate origin is located on the bottom wall under the center of the bump and the Reynolds number based on the bulk velocity (0.83 m/s), and the bump height is 16,000.

The same flow solver, CharLES with a Voronoi mesh generator from Cascade Technologies, is used. The boundary conditions for the skewed bump are similar to those of

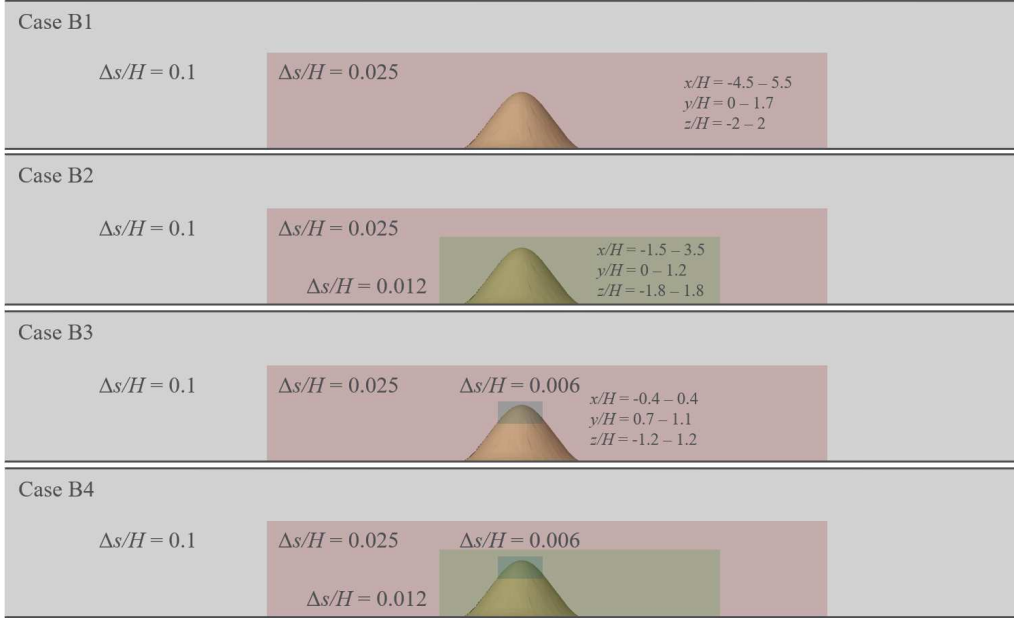


FIGURE 6. Schematic diagram of the mesh refinement.

the bent square duct (see Section 2.1). At the inlet, a synthetic turbulence boundary condition is utilized and the Navier-Stokes characteristic boundary condition is imposed at the outlet. The ODE-based equilibrium wall model (Kawai & Larsson 2012) is used to obtain the wall shear stress on the isothermal bottom, top, and side walls.

The computational domain size is $(L_x \times L_y \times L_z) = (575.7 \text{ mm} \times 50 \text{ mm} \times 100 \text{ mm})$. We consider four different sets of grid resolutions as shown in Table 2 and Figure 6 to investigate which region needs to be refined to capture the correct flow physics. For all the cases, the coarsest grid resolution is set to $0.1H$, and the meshes are refined around the bump and the bottom wall $(-4.5H < x < 5.5H, 0 < y < 1.7H, -2H < z < 2H)$, see red-colored region in Figure 6) such that the grid size in that region is set to $0.025H$. This refinement results in 20 grid cells across the boundary layer thickness at $x/H = -4$. For case B2, an additional refinement window with the grid size of $0.012H$ is added to the case B1 around the bump and the bottom wall $(-1.5H < x < 3.5H, 0 < y < 1.2H, -1.8H < z < 1.8H)$, see green-colored region in Figure 6). For case B3, the refinement window with the grid size of $0.006H$ is added to the case B1 on top of the bump $(-0.4H < x < 0.4H, 0.7 < y < 1.1H, -1.2H < z < 1.2H)$, see blue-colored region in Figure 6). Lastly for the case B4, both refinement windows used for each case B2 and B3, respectively, are included into case B1 to assess grid convergence.

3.2. Results and discussion

In Figure 7 shows the mean streamwise velocity contours on the centerplane (i.e., $z/H = 0$) from case B3. The flow separates near the top of the bump ($x/H \sim 0$) and reattaches around $x/H = 2$, generating a large separation bubble behind the bump. Note that case B2 is set to contain the main separation bubble within the green-colored refined region and the case B3 is set to include additional grid cells around the separation point..

Figures 8, 9, and 10 show the mean streamwise velocity profiles at various streamwise locations from the present WMLES along with the reference experiment and LES data

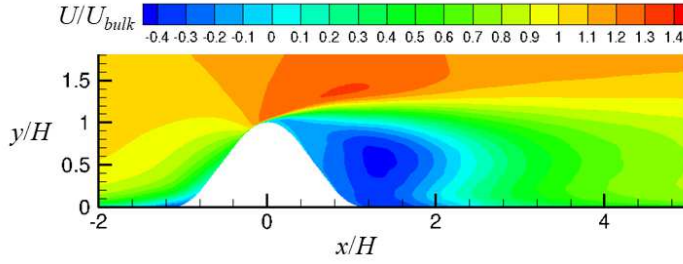


FIGURE 7. Contours of mean streamwise velocity at $z/H = 0$ from the case B3.

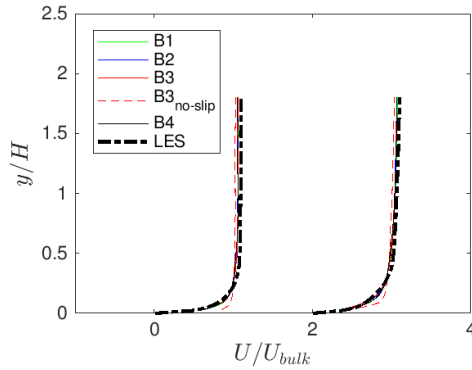


FIGURE 8. Mean velocity profiles in the upstream section of the bump at $x/H = -4$ and -2 . Here, the profile at $x/H = -2$ is shifted by 2 on the horizontal axis. Lines, present WMLES (cases B1,B2,B3,B4); dashed lines, no-slip LES on the case B3 mesh (without wall model); dash-dot lines, LES (Ching & Eaton 2019).

(Ching *et al.* 2018a; Ching & Eaton 2019). Before the flow separates around the top of the bump (i.e., at the upstream section of the bump (Figure 8) and the windward side of the bump (Figure 9(a))), the present WMLES predicts reasonable velocity profiles regardless of the mesh distribution. This result indicates that the mean velocity at the upstream section of the bump at $x/H = -4$ can be generated by using the synthetic turbulence boundary condition as the inlet boundary condition for all the grid resolutions considered. On the other hand, the velocity profiles at the leeward side of the bump (Figure 9 (b)) and at $x/H = 3$ in the downstream section of the bump (Figure 10) are sensitive to the grid resolution. In case B1, the mean velocity distributions at the leeward side of the bump (Figure 9(b)) and at $x/H = 3$ (Figure 10) do not agree well with the reference experiment and LES. These locations are inside the main separation bubble and right behind the bubble, respectively, where the prediction using WMLES is the most challenging. However, with the additional grid refinement (cases B2-B4), the discrepancy between the WMLES and reference cases is greatly reduced; the profiles from the cases B3 and B4 show an excellent agreement with the reference LES and experiments. Note that the prediction of the velocity profile from the case B3 is improved at $x/H = 3$ compared to that of the case B1 even though the mesh is not refined there. Finally, in the far downstream of the separation bubble at $x/H = 5$, the effect of the 3D separation is weakened and again the present WMLES can predict reasonable velocity profiles for all mesh resolutions.

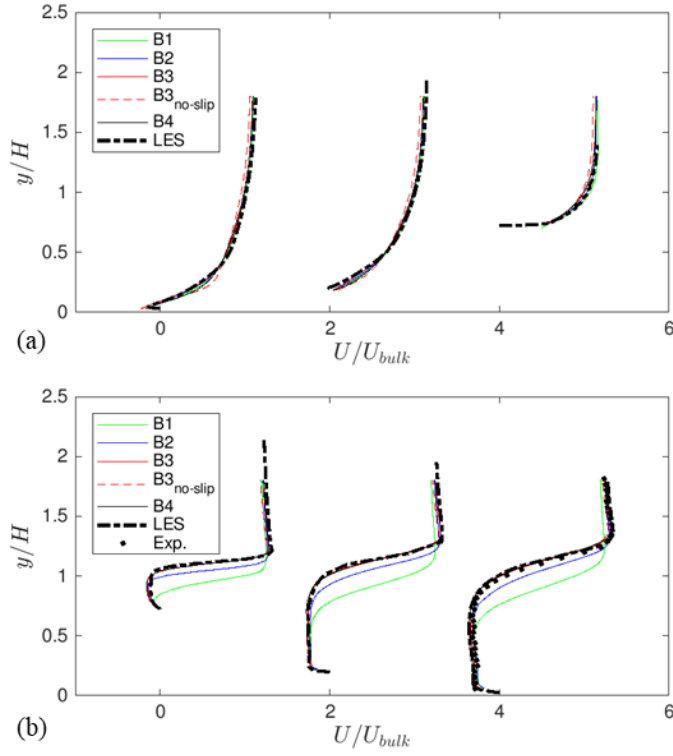


FIGURE 9. Mean velocity profiles over the bump: (a) windward side at $x/H = -1, -0.8$, and -0.4 ; (b) leeward side at $x/H = 0.4, 0.8$, and 1 . Here, the profiles at $x/H = -0.8$ and 0.8 are shifted by 2 and the profiles at $x/H = -0.4$ and 1 are shifted by 4 on the horizontal axis, respectively. Lines, present WMLES (cases B1,B2,B3,B4); dashed lines, no-slip LES on the case B3 mesh (without wall model); dash-dot lines, LES (Ching & Eaton 2019); circles, experiment (Ching *et al.* 2018a).

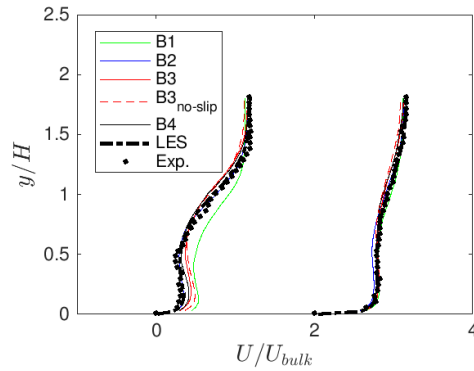


FIGURE 10. Mean velocity profiles in the downstream section of the bump at $x/H = 3$ and 5 . Here, the profile at $x/H = 5$ is shifted by 2 on the horizontal axis. Lines, present WMLES (cases B1,B2,B3,B4); dashed lines, no-slip LES on the case B3 mesh (without wall model); dash-dot lines, LES (Ching & Eaton 2019); circles, experiment (Ching *et al.* 2018a).

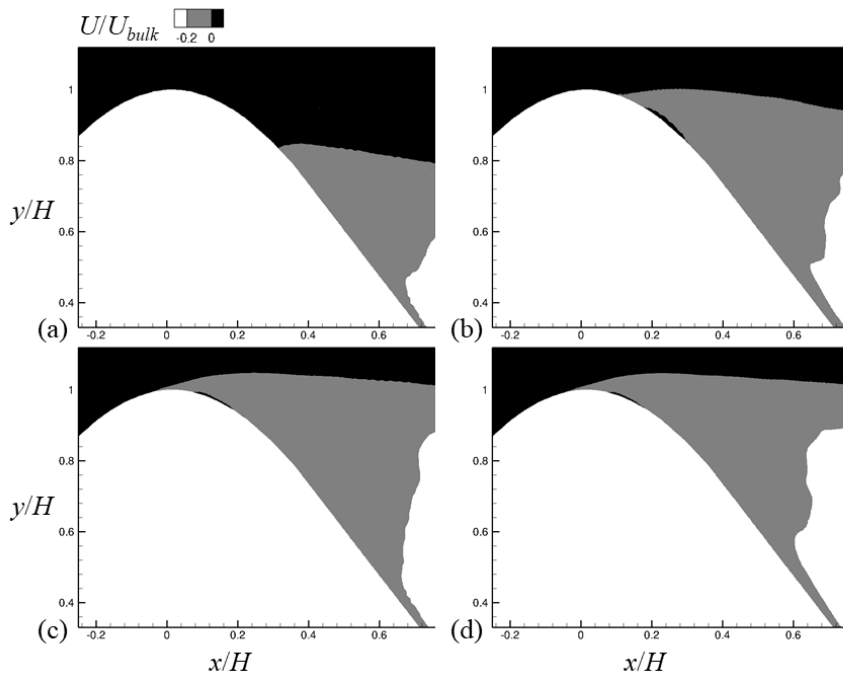


FIGURE 11. Contours of mean streamwise velocity at $z/H = 0$ showing the separation point and the secondary separation bubble: (a) case B1; (b) case B2; (c) case B3; (d) case B4.

The velocity profiles from the no-slip LES (i.e., without the wall model) on the case B3 mesh are also indicated as the red dashed lines in Figures 8, 9, and 10. In the upstream section of the bump (Figure 8), these red dashed lines deviates slightly from the WMLES and experimental results in the near-wall region. However, velocity profiles over the bump (Figure 9) predicted from the no-slip LES are almost on top of the red solid lines, i.e., the equilibrium wall model does not influence this region. The results from the 3D separating and reattaching flows are different from the previously reported 2D separating and reattaching flows (Park 2017), showing that the no-slip LES with the coarse mesh significantly underperforms the WMLES. Park (2017) reported the performance of WMLES of the flow over the NASA hump, where the wall-mounted hump geometry was homogeneous in the spanwise direction. Here, the flow over the hump separates around the apex of the hump because of the sharp curvature change. Therefore, the separation point for the NASA hump was determined by the hump geometry, unlike the present study. Here, the separation is caused by the development of an adverse pressure gradient. Consequently, the grid restriction for the current 3D separating and reattaching flows is more strict than that for the NASA hump configuration. More importantly, this result indicates that the use of the equilibrium wall model in the 3D separated region does not hinder the performance of WMLES and switching the wall boundary condition from the wall shear stress boundary condition to the no-slip boundary condition might not be necessary if a sufficiently dense grid resolution is provided around the separation point (case B3). Hence, the use of the wall shear stress boundary condition across the full domain might be justified in the 3D separated flows similar to the present one. Right

after the separation bubble at $x/H = 3$, no-slip LES slightly underperforms the WMLES, but this deviation becomes marginal at $x/H = 5$ in Figure 10.

Figure 11 shows a zoomed-in view of the streamwise velocity contours at $z/H = 0$ from cases B1-B4 of the present WMLES. In the reference LES study (Ching & Eaton 2019), the separation point on the centerplane was shown to be located around $x/H = 0$. Here, this separation point is not well predicted from the cases B1 and B2, whereas that from the cases B3 and B4 is similar to the LES result. In addition to the large separation bubble, the thin secondary separation bubble was also observed at the leeside of the bump in the previous LES study by Ching & Eaton (2019). These secondary separation bubbles are captured in Figure 11 in the range of $0.1 < x/H < 0.3$ for cases B2-B4. However, their size and location do not match accurately with those from the LES study because this secondary bubble is too thin to be captured with the coarse mesh resolution used in the current WMLES.

The statistics from case B3 with 10.8 million control volumes are comparable to those from the case B4 with 22.3 million control volumes as well as those from the reference studies. This similarity reveals that the mesh resolution around the 3D separation point (i.e., the blue refinement window in Figure 6) plays an important role in the successful prediction of the 3D separated flows using the equilibrium wall model.

Figure 12 illustrates the vortex structures behind the bump. As was reported in the previous series of papers (Ching *et al.* 2018a,b; Ching & Eaton 2019), a common-up vortex pair is captured right behind the bump (Figure 12(a)) which evolves into a common-down vortex pair in the far downstream (Figure 12(c)). Not only the mean structures, but also the dynamics of flow structures behind the bump are well captured from the current WMLES. Figure 13 shows velocity power spectra from three probes in the wake region. Following the references (Ching *et al.* 2018a; Ching & Eaton 2019), the Strouhal number is defined as

$$St = \frac{f(A_b)^{0.5}}{U_{bulk}}, \quad (3.4)$$

where f is the shedding frequency, A_b is the blockage area, and U_{bulk} is the bulk velocity. The shedding frequency from the WMLES matches with the reference LES, indicating that the current WMLES is able to predict both the statistics and dynamics of the flow over the skewed bump with reasonable accuracy.

4. Conclusions

We conducted WMLES to examine the performance of a simple and widely used ODE-based equilibrium wall model in a spatially-developing 3D TBL inside a bent square duct (Schwarz & Bradshaw 1994) and 3D separated flows behind a skewed bump (Ching *et al.* 2018a,b; Ching & Eaton 2019). From the square duct simulation, the mean velocity profiles and crossflow angles in the outer region were predicted with high accuracy for all the considered mesh resolutions. Some disagreement was observed in the crossflow angles in the bend region where the non-equilibrium effect is most significant. Also, the simulation for the wall-mounted skewed bump showed that this simple ODE-based equilibrium wall model along with an adequate grid resolution around the 3D separation point resulted in reasonable predictions of 3D separating and reattaching flows, including mean velocity distributions, separation bubbles, and vortex structures in the bump wake.

From the present study, we have demonstrated the potential of the ODE-based equilibrium wall model for practical LES with relatively complex flow configurations, despite

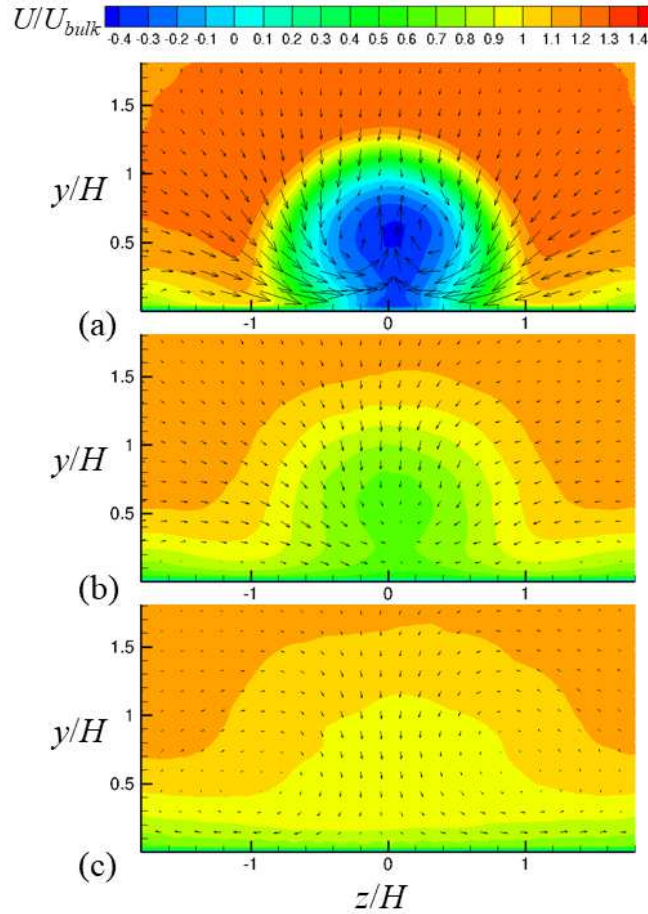


FIGURE 12. Mean streamwise velocity contours with in-plane velocity vectors from the case B3: (a) $x/H = 1.5$; (b) $x/H = 4$; (c) $x/H = 8$.

its low computational complexity and underlying equilibrium assumptions. It was also shown that the use of wall shear stress boundary conditions across the whole domain for 3D separated flows (without switching to the no-slip condition) does not hinder the performance of WMLES.

Acknowledgments

This investigation was funded by ONR Grant No. N00014-16-S-BA10. MC is grateful to Dr. David S. Ching for providing the LES data.

REFERENCES

- BAE, H. J., LOZANO-DURÁN, A., BOSE, S. T. & MOIN, P. 2018 Dynamic slip wall model for large-eddy simulation. *J. Fluid Mech.* **859**, 400–432.
- BOSE, S. T. & PARK, G. I. 2018 Wall-modeled large-eddy simulation for complex turbulent flows. *Annu. Rev. Fluid Mech.* **5**, 535–561.

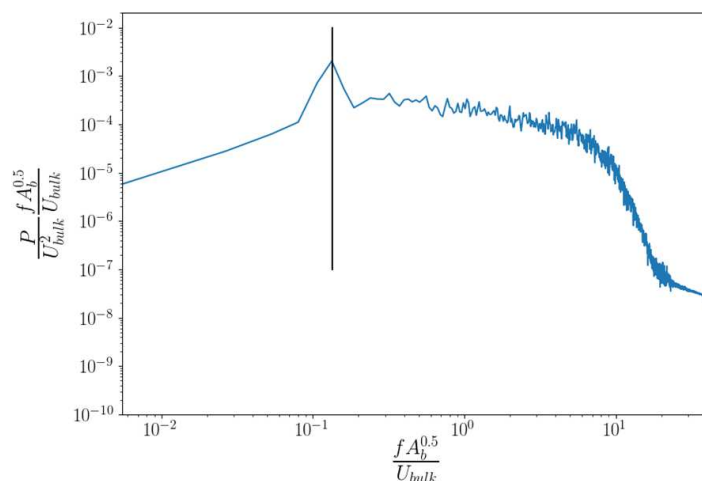


FIGURE 13. Velocity power spectra in the wake region from the case B3. The vertical line denotes Strouhal number from LES (Ching & Eaton 2019).

- BRÈS, G. A., BOSE, S. T., EMORY, M., HAM, F. E., SCHMIDT, O. T., RIGAS, G. & COLONIUS, T. 2018 Large-eddy simulations of co-annular turbulent jet using a Voronoi-based mesh generation framework. *AIAA Paper* 2018-3302.
- CHAPMAN, D. R. 1979 Computational aerodynamics development and outlook. *AIAA J.* **17**, 1293–1313.
- CHING, D. S., ELKINS, C. J. & EATON, J. K. 2018 Investigation of geometric sensitivity of a non-axisymmetric bump: 3D mean velocity measurements *Exp. Fluids* **59**, 1–14.
- CHING, D. S., ELKINS, C. J., ALLEY, M. T. & EATON, J. K. 2018 Unsteady vortex structures in the wake of nonaxisymmetric bumps using spiral MRV *Exp. Fluids* **59**, 1–17.
- CHING, D. S. & EATON, J. K. 2019 LES study of unsteady wake dynamics and geometric sensitivity on a skewed bump *J. Fluid Mech.* Submitted.
- CHO, M., PARK, G. I. & MOIN, P. 2018 Wall-modeled LES of a spatially-developing non-equilibrium turbulent boundary layer. *Annual Research Briefs*, Center for Turbulence Research, Stanford University, pp. 251-259.
- CHOI, H. & MOIN, P. 2012 Grid-point requirements for large eddy simulation: Chapman's estimates revisited. *Phys. Fluids* **24**, 011702.
- GIOMETTO, M. G., LOZANO-DURÁN, A., PARK, G. I. & MOIN, P. 2017 Three-dimensional transient channel flow at moderate Reynolds numbers: Analysis and wall modeling. *Annual Research Briefs*, Center for Turbulence Research, Stanford University, pp. 193-205.
- KAWAI, S. & LARSSON, J. 2012 Wall-modeling in large eddy simulation: length scales, grid resolution, and accuracy. *Phys. Fluids* **24**, 015015.
- LOZANO-DURÁN, A., GIOMETTO, M. G., PARK, G. I. & MOIN, P. 2020 Non-equilibrium three-dimensional boundary layers at moderate Reynolds numbers. *J. Fluid Mech.* **883**, A20.
- PARK, G. I. & MOIN, P. 2014 An improved dynamic non-equilibrium wall-model for large eddy simulation. *Phys. Fluids* **26**, 015108.

- PARK, G. I. 2017 Wall-modeled large-eddy simulation of a high Reynolds number separating and reattaching flow. *AIAA J.* **55**, 3709–3721.
- POINSOT, T. & LELE, S. K. 1992 Boundary conditions for direct simulation of compressible viscous flows *J. Comput. Phys.* **101**, 104–129.
- SCHWARZ, W. R. & BRADSHAW, P. 1994 Turbulence structural changes for a three-dimensional turbulent boundary layer in a 30° bend *J. Fluid Mech.* **272**, 183–209.
- SLOTNICK, J., KHODADOUST, A., ALONSO, J., DARMOFAL, D., GROPP, W., LURIE, E. & MAVRIPLIS, D. 2014 CFD Vision 2030 Study: A Path to Revolutionary Computational Aerosciences. *NASA/CR-2014-218178*, 1–51.
- YANG, X. I. A., SADIQUE, J., MITTAL, R. & MENEVEAU, C. 2015 Integral wall model for large eddy simulations of wall-bounded turbulent flows. *Phys. Fluids* **27**, 025112.
- YANG, X. I. A., PARK, G. I. & MOIN, P. 2017 Log-layer mismatch and modeling of the fluctuating wall stress in wall-modeled large-eddy simulations *Phys. Rev. Fluids* **2**, 104601.